ARTICLES
https://doi.org/10.1038/s41929-018-0199-x
nature catalysis

Catalytic CO_2 reduction by palladium-decorated silicon–hydride nanosheets

Chenxi Qian[1,5], Wei Sun[1,5], Darius L. H. Hung[1], Chenyue Qiu[2], Meysam Makaremi[2], Sai Govind Hari Kumar[1], Lili Wan[1,3], Mireille Ghoussoub[1], Thomas E. Wood[1,4], Meikun Xia[1], Athanasios A. Tountas[1], Young Feng Li[1], Lu Wang[1], Yuchan Dong[1], Ilya Gourevich[1], Chandra Veer Singh[2*] and Geoffrey A. Ozin[1*]

Heterogeneous conversion of CO_2 to fuels by Si surface hydrides has recently attracted broad research interest. Being earth-abundant, low-cost and non-toxic, elemental Si is a very attractive candidate for this process, which targets CO_2 conversion to synthetic fuels on a gigatonne-per-year scale. It is well known, however, that silicon hydrides react stoichiometrically with CO_2, and all attempts have failed to achieve catalytic conversion. The problem originates from the formation of inactive silanols and siloxanes with permanent loss of Si hydrides. Here, we deposit Pd on the surface of Si nanosheets, aiming to address the core of the problem. An operando infrared study shows Si hydrides successfully regenerating on such surfaces exposed to CO_2 and H_2. We demonstrate that silicon–hydride nanosheets decorated with Pd nanoparticles can enable the reverse water–gas shift reaction in a catalytic cycle.

Gigatonne-per-year conversion of CO_2 into synthetic fuels will require a technology able to function at this massive scale[1–4]. Heterogeneous catalytic hydrogenation of CO_2 is one of the few approaches that has the potential to achieve this impressive feat, but it will require huge amounts of catalyst to facilitate CO_2 conversion on this grand scale. Therefore, the earth abundance, cost and toxicity of the elements comprising the catalyst become determining factors for successful implementation of the process. Silicon would be one perfect choice on all three counts.

Molecular silanes are known to convert CO_2 to its reduced forms. Silane (SiH_4), for example, as the simplest form in the family of silanes, burns in CO_2. The combustion products are carbon and silicon dioxide[5]. Silanes can convert CO_2 into methanol or methane with the assistance of some catalysts[6–8]. As the form of Si evolves from molecules to clusters to nanocrystals, the surface hydrides become less reactive. Recent studies have shown evidence that the hydrides of nanoscale Si materials are capable of reducing CO_2. Veinot and colleagues reported that surface silicon hydrides, as in solution-phase colloids, could convert CO_2 to formaldehyde under high pressure and high temperature[9]. Ozin and co-workers reported one of the earliest observations of gas-phase reactivity of surface silicon hydrides towards CO_2 reduction, using 3 nm Si nanocrystals. The reduction product was CO, as confirmed by ^{13}C experiments[10,11]. In another study by Veinot et al., the surface hydrides of high-surface-area porous Si nanoparticles were proven to convert CO_2 to methanol[12]. These demonstrations have explored the possibilities of CO_2 conversion using Si materials as the reducing agent, boasting a promising, low-cost solution to making value-added chemicals and fuels from CO_2 and energy inputs such as sunlight.

The problem, however, is that Si, in any of its known forms, has never been shown to function as a catalyst for hydrogenating CO_2. As described above, all attempts so far to achieve this goal have resulted in stoichiometric reactions, because the Si deactivates by formation of inactive surface silanols (Si–OH) and siloxane (Si–O–Si) groups[10,12]. How to restore the surface hydrides in the CO_2 conversion process poses the key challenge in turning this stoichiometric reaction into a catalytic reaction.

In this Article we describe how we take on this challenge and resolve the problem by learning how to reinstate the surface silicon hydrides. We designed an innovative method to synthesize metal-nanoparticle-decorated two-dimensional Si nanosheets. We demonstrate that nanosheets of hydride-capped Si decorated with Pd nanoparticles can enable the reverse water gas shift reaction in a catalytic fashion, under light irradiation. With evidence from in situ isotope-labelling infrared studies and support from theoretical calculations, we acquired a clear and fundamental understanding on the newfound missing piece in the puzzle of the catalytic cycle, which also gives us a unique insight into the Si surface chemistry and inspires future designs of Si-based catalyst systems.

Results

Materials design and characterizations. Silicon nanosheets were exfoliated from bulk calcium silicide with a previously reported method[13]. The exfoliated Si nanosheets were treated with aqueous hydrofluoric acid, so that the oxides formed during the exfoliation process were removed and the resulting exposed surface was all silicon hydrides. A dispersion of the fresh hydride-terminated Si nanosheets was then mixed with a palladium acetate solution. This enabled palladium nanoparticle growth on the Si nanosheet surface (denoted Pd@SiNS, Fig. 1a). During the growth of palladium nanoparticles (NP), some of the surface silicon hydrides on the nanosheets (NS) reduce the solution-phase Pd(II), converting them into surface Pd(0). This innovative and facile method of in situ metal nanoparticle synthesis utilizes some of the surface

[1]Materials Chemistry and Nanochemistry Research Group, Solar Fuels Cluster, Department of Chemistry, University of Toronto, Toronto, Ontario, Canada. [2]Department of Materials Science and Engineering, University of Toronto, Toronto, Ontario, Canada. [3]College of Environmental Science and Engineering, Nankai University, Tianjin, China. [4]Department of Chemical Engineering and Applied Chemistry, University of Toronto, Toronto, Ontario, Canada. [5]These authors contributed equally: Chenxi Qian and Wei Sun. *e-mail: chandraveer.singh@utoronto.ca; gozin@chem.utoronto.ca

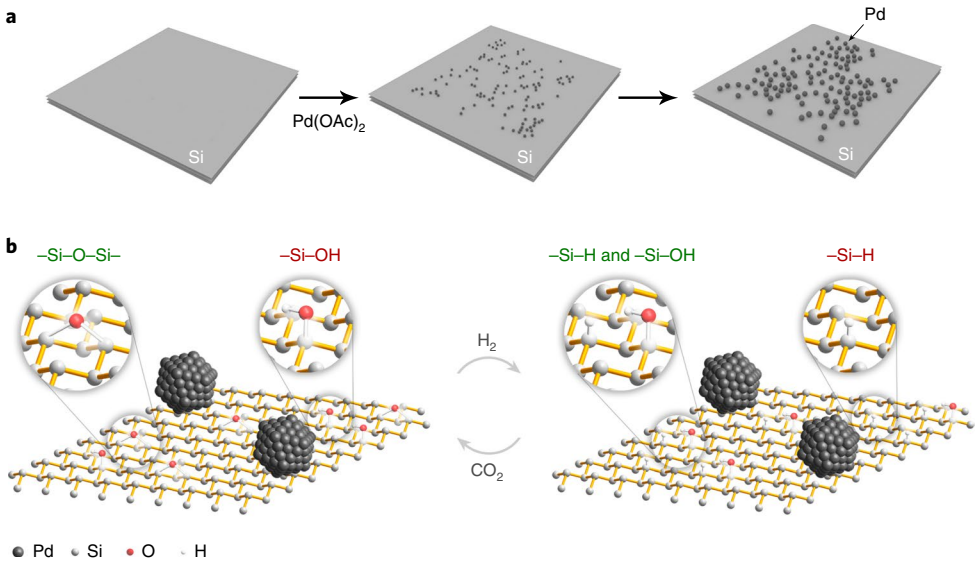

Fig. 1 | Preparation and surface chemistry of Pd@SiNS. a, Illustration of Pd nanoparticle growth on Si nanosheets: fresh (hydride-terminated) Si nanosheets were immersed in palladium acetate solution, enabling the reduction of Pd(II) to Pd(0) on the surface. **b**, Schematics of the surface chemistry of Pd@SiNS during the catalytic CO_2 reduction reaction. Left, An oxidized state of Pd@SiNS, with –Si–O–Si– and –Si–OH as the abundant surface species. Right, A reduced state of Pd@SiNS, with –Si–H/–Si–OH (reduced from –Si–O–Si–) and –Si–H (reduced from –Si–OH) as the dominant surface species. Characterization of the as-prepared Pd@SiNS sample confirms it to be in an oxidized state. Typically, every Si atom is connected to three other Si atoms and a fourth bond (–H, –OH or –O–Si–), omitted in the schematics for simplicity unless specified.

silicon hydrides as the reducing agent, with the remainder used for CO_2 reduction. We also demonstrated the feasibility of depositing other metals on the Si nanosheet surface, such as gold (Supplementary Fig. 1). Different from conventional methods of doping Si nanostructures by incorporating transition metals in the precursor via thermal treatment[14], our synthesis is carried out at room temperature. As a general synthetic route, it is not limited to NP@NS, but is applicable to other heterostructures as well, such as NP@NP[15]. This method yields highly dispersed and immobilized metal nanoparticles on the Si hydride surface. The method creates a new class of materials that are not only useful as efficient catalysts, but also possibly functional in other applications, such as the surface signal enhancement techniques, and new photothermal systems.

The structure of SiNS and Pd@SiNS (0.5% mass loading) samples were confirmed by powder X-ray diffraction (PXRD) (Supplementary Fig. 2). Proof of the Pd@SiNS growth mechanism was provided by Fourier-transform infrared (FTIR) spectroscopy (Fig. 2a). Before deposition of Pd, there are prominent peaks at ~2,100 cm^{-1} and 900 cm^{-1}, corresponding to Si–H stretching and scissoring modes, respectively. After Pd deposition, the sample contained less Si–H but acquired more Si–O, shown by dominant peaks at ~1,057 cm^{-1} and 840 cm^{-1}. These FTIR results correspond well with our model, as schematized in Fig. 1b (left), where the surface of a Si nanosheet has an abundance of Si–O–Si and Si–O–H species. X-ray photoelectron spectroscopy (XPS) (Fig. 2b,c) provided more detailed information about Pd@SiNS. The Si 2*p* spectrum shows two kinds of peak at binding energies of ~99 eV and 103 eV, corresponding to the backbone Si in the 2D network and the oxidized Si, respectively. The palladium deposited on the nanosheet surface is mainly zero-valent Pd, as seen in the Pd 3*d* spectrum (Pd $3d_{5/2}$ and Pd $3d_{3/2}$ peaks, at 335 eV and 340 eV, respectively). Diffuse reflectance spectra of the pristine SiNS and Pd@SiNS samples showed slightly different band-edge absorptions, indicating the difference in the degree of oxidation in each sample, as well as the successful incorporation of Pd in the Pd@SiNS sample (due to the absorption of Pd; Supplementary Fig. 3).

A scanning transmission electron microscopy (STEM) image (Fig. 2d) shows a typical Si nanosheet covered by Pd nanoparticles synthesized by this method. The size of the Pd nanoparticles is ~5 nm. Figure 2e presents a high-resolution transmission electron microscopy (HRTEM) image showing clear lattice spacings of Pd [111], Pd [200] in the darker (high-*Z*, *Z*=atomic number) region (0.23 nm and 0.20 nm) and Si [111] in the brighter (low-*Z*, *Z*=atomic number) background (0.31 nm). By limiting the amount of Pd to 0.5% (mass loading as reference to Si) we obtained a clear energy-dispersive X-ray (EDX) mapping of the sample surface to identify these high-*Z*-contrast dots in the images as Pd nanoparticles, and the low-*Z*-contrast background as Si nanosheets (Fig. 2f–h). A Brunauer–Emmett–Teller (BET) surface area of 197 $m^2 g^{-1}$ was measured for Pd@SiNS (0.5% mass loading of Pd). In comparison, the pristine SiNS had a BET surface area of 77 $m^2 g^{-1}$. The BET N_2 adsorption plots are shown in Supplementary Fig. 4. The surface area was more than doubled by Pd deposition. A quick calculation shows that 0.5% Pd by weight makes a negligible contribution (less than 0.5%) to the surface area increase. An explanation for the surface area increase is that the Pd metal nanoparticles act as separators and significantly reduce the interlayer stacking forces between the Si nanosheets (as seen in the STEM images in Supplementary Fig. 5, the pristine SiNS has a multilayered or bulky structure while Pd@SiNS is imaged as thin layers). This indicates that, by the strategy of metal deposition, not only can we obtain highly dispersed, immobilized metal nanoparticles decorated on the support surface, but we can also achieve a higher surface area with less stacked sheets.

CO_2 reduction performance. The $^{13}CO_2/H_2$ reactivity over the Pd@SiNS sample was tested in a batch reactor. The Pd@SiNS sample was dropcast onto a borosilicate glass microfibre filter substrate before testing in the reactor. The reactor had a total pressure of ~27 p.s.i. (filled by $^{13}CO_2$ and H_2 at a 1:1 ratio) and was irradiated with a 300 W Xe lamp (~15 suns). The reaction temperature was held constant at 170 °C. The reaction time was 2.3 h for each run. A total of 15 consecutive runs were performed. In these runs, ^{13}CO was detected as the only reduction product. This was consistent with the $^{13}CO_2/H_2$

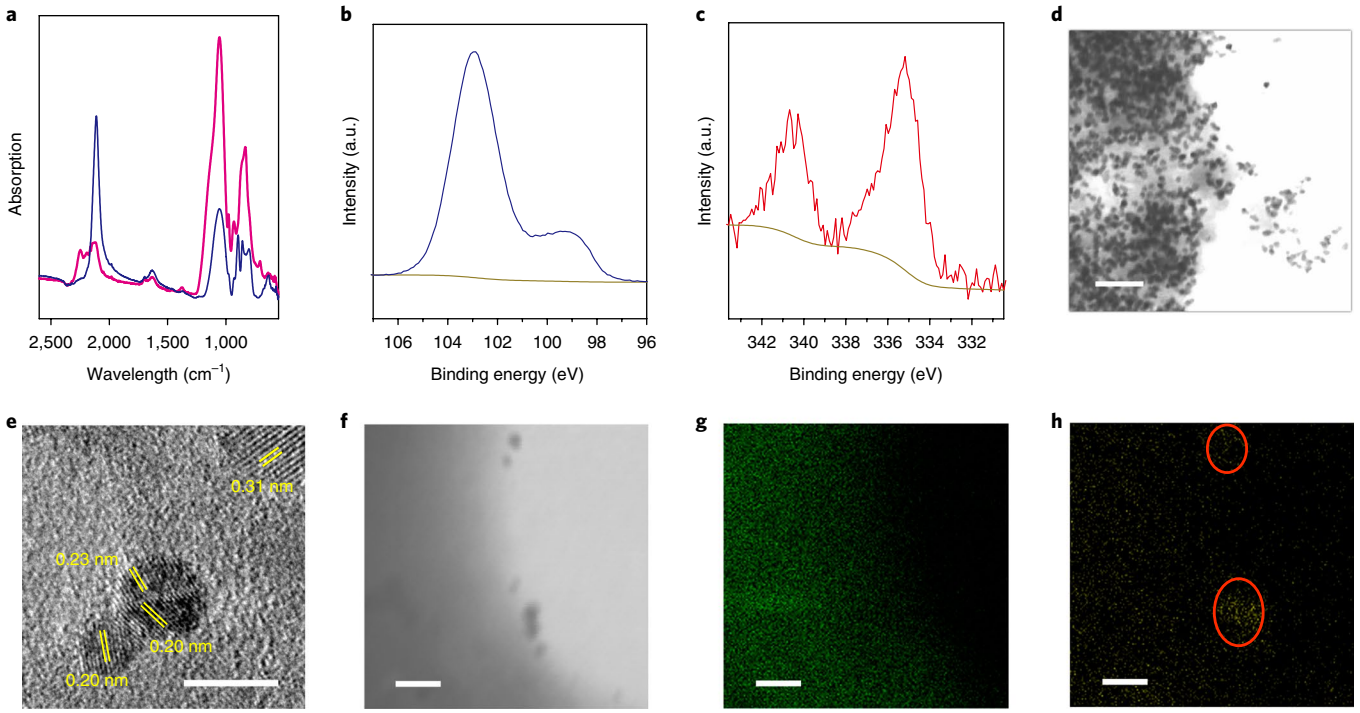

Fig. 2 | Materials characterization. a, FTIR spectra of Si nanosheets before (blue) and after (pink) Pd deposition. The spectra indicate that silicon hydrides are consumed, while silicon hydroxides/oxides are formed. **b**, XPS study on the Pd@SiNS sample shows Si 2*p* peaks at mainly two binding energy regions, corresponding to oxidized Si and the unoxidized backbone Si nanosheet Si. **c**, Pd 3*d* XPS spectra show that most of the Pd in the Pd@SiNS sample is elemental Pd, with a small portion oxidized to Pd(II), if finely fitted. **d**, STEM image of a Pd@SiNS sample. Scale bar, 50 nm. **e**, A typical HRTEM image of a Pd@SiNS sample, showing the lattice spacings of Pd [111], Pd [200] in the darker region (0.23 nm and 0.20 nm) and Si [111] in the brighter background (0.31 nm). Scale bar, 5 nm. **f–h**, STEM image and EDX mapping of a Pd@SiNS sample. Scale bars, 20 nm (**f–h**). Identifiable Si sheet in green (**g**) and Pd particles in yellow (circled in **h**).

reactivity over hydride-terminated Si nanocrystals (ncSi:H), as previously reported by us[10]. Similarly, in both cases, the key step of CO_2 reduction is identified as the oxidation of the surface hydrides:

$$CO_2 + {-}Si:H \rightarrow CO + {-}Si:(O)H \quad (1)$$

However, for Pd@SiNS (as a catalyst), distinct from ncSi:H (as a stoichiometric reducing agent), what follows this key reduction step becomes another story. For ncSi:H, as the surface is oxidized, the reducing agent turns out to be inactive. For the Pd@SiNS sample tested, after the initial three runs, the ^{13}CO production rate was essentially stable at ~10,000 nmol (g cat)$^{-1}$ h^{-1}. The underlying reason was that the surface hydride was replenished by a H$^{\cdot}$ source provided by Pd nanoparticles on the nanosheet surface. This H$^{\cdot}$ source also kept the original silicon hydride sites from being oxidized.

$$-Si^{\cdot} + H^{\cdot} \rightarrow -Si:H \quad (2)$$

$$-Si:(O)H + 2H^{\cdot} \rightarrow -Si:H + H_2 \quad (3)$$

These are the key steps involved in the process. A detailed mechanism and experimental support will be elaborated later in this Article, associated with a carefully designed in situ infrared study. The ^{13}CO production rates in the initial runs were high, owing to a high initial hydride stock on the Si nanosheets. Due to the heterogeneity of the Pd@SiNS morphology and structure, part of the stock has no access to the H$^{\cdot}$ source (in the vicinity of Pd nanoparticles). These hydrides were consumed permanently in the initial runs, as described in equation (1). In the following runs Pd@SiNS was fully operational as a catalyst and the ^{13}CO production rates were quite high and stable (black line, Fig. 3a). We attained a turnover number (TON) of 420 with the data from the first 15 runs in the batch reactor, which also strongly suggested that the reaction was catalytic (for calculation see Supplementary Note 1). To check the reactivity of the catalysts over more consecutive runs, we conducted flow reactor experiments on the same sample with similar conditions as the batch tests. The results (black line in Supplementary Fig. 6) showed a stable CO_2 reduction rate up to 50 runs (50 h).

Moreover, when we increased the mass loading of Pd from 0.5% to 2%, there was also a fourfold increase in the stable rate observed. These observations strongly support our observation that the CO_2 reduction over Pd@SiNS was a catalytic process, and that the interface between Pd and Si is actively involved in this process.

As a control experiment, freshly etched Si nanosheets (pristine SiNS) were dropcast onto a borosilicate glass microfibre filter substrate and put into the same batch reactor for testing, under the same conditions. The mass of SiNS used was the same as that of Pd@SiNS. The SiNS sample was tested for 15 consecutive runs. As early as the fourth run, the rate started to drop and showed clear signs of sample deactivation (red line, Fig. 3a). In comparison, the ^{13}CO production rate of the first run hit the 74,000 nmol (g cat)$^{-1}$ h^{-1} bar, much higher than the first-run rate in the Pd@SiNS case. This is because the SiNS always had a much larger initial hydride reservoir than Pd@SiNS, as confirmed earlier by the FTIR characterization (Fig. 2a). Starting from the second run, the ^{13}CO production rates underwent huge drops. It then reached a plateau at a few percent of the final stable rates in the Pd@SiNS case. A high initial hydride stock yielded low final ^{13}CO production rates, suggesting that the underlying CO_2 reduction mechanism was different for the pristine SiNS. In fact, the pristine hydride-terminated SiNS bears many similarities to the previously reported ncSi:H (ref. [10]). The CO_2 reduction reaction was still stoichiometric in this case.

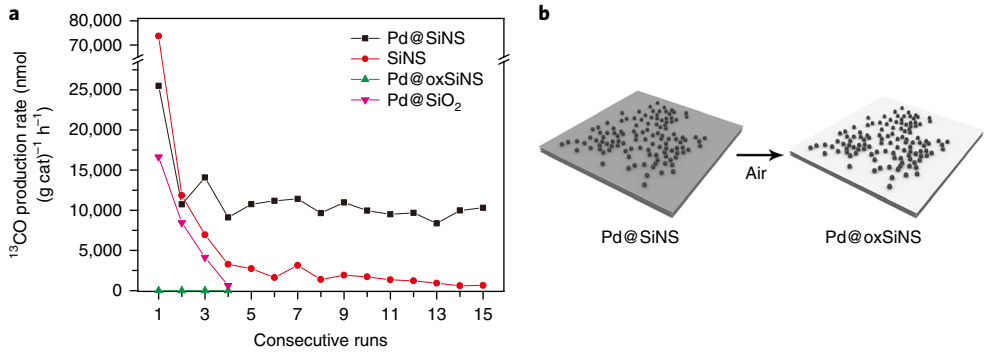

Fig. 3 | CO_2 reduction performance. a, ^{13}CO production rate of four samples, Pd@SiNS, pristine SiNS, Pd@oxSiNS (Pd nanoparticles on fully oxidized Si nanosheets) and Pd@SiO_2 (Pd nanoparticles on silica), under the following conditions: (1) exposure to a mixture of $^{13}CO_2$ and H_2 (1:1 molar ratio) in the batch reactor; (2) reaction temperature of 170 °C; (3) illumination by a 300 W Xe lamp with a light intensity of ~15 suns; (4) a reaction time for each run of 2.3 h. In a series of consecutive runs, the sample remained in the reactor and the gases used in each run were fresh feeds. **b**, Preparation of the control sample Pd@oxSiNS. The Pd@oxSiNS was prepared from the as-tested Pd@SiNS on the original borosilicate glass fibre filter to guarantee that the control experiment was valid.

To prove that the catalytic reactivity of Pd@SiNS is a synergetic effect of both Pd and SiNS, but not the sole effect of the Pd nanoparticles themselves, we performed another control experiment in which we focused on the reactivity of Pd. The as-tested Pd@SiNS sample on the glass fibre filter with a stable ^{13}CO production rate was taken out of the reactor and subsequently placed in ambient air, with moderate ambient light for a quick oxidation. After 3 days, the colour of the sample turned from yellow-green to white-grey. Pd@SiNS became Pd nanoparticles on fully oxidized SiNS (Pd@oxSiNS), as illustrated in Fig. 3b. Pd@oxSiNS was then essentially a mixture of the Pd nanoparticles and catalytically inactive silicon dioxide, while retaining exactly the same amount, size, morphology and geometric distribution of the Pd nanoparticles as in the original Pd@SiNS sample. This method validated the control experiment. If the Pd nanoparticles were simultaneously oxidized in the process, they will be quickly reinstated to the reduced form of Pd metal when placed in the H_2-containing atmosphere under the reactor conditions. The testing results for Pd@oxSiNS showed zero ^{13}CO production rate. This suggests that Pd nanoparticles alone had no contribution to the CO_2 reduction under reactor conditions. Another control experiment carried out on Pd@SiO_2 (similar-sized Pd nanoparticles on a SiO_2 support, with the same 0.5% mass loading) showed a fast decline in the ^{13}CO production rate, with the fourth run reaching close to zero (pink line, Fig. 3a). This suggests that Pd with a similar size and amount on such supports would not be a stable catalyst under our reaction conditions. In this case, the active sites are on the Pd nanoparticles and this deactivation results from various physical and chemical changes of the Pd[16,17]. This result also corresponds well with previous reports. Among many on oxide-supported metal catalysts[18], the 3.3 nm Pd on SiO_2 (3 wt%) shows nearly 0% conversion below 300 °C (ref. [19]). It is therefore apparent that our Pd@SiNS is fundamentally different from the traditional oxide-supported Pd catalysts.

Conclusively, only Pd@SiNS appeared to have catalytically active silicon hydrides, and the reactivity arises from a synergy of Pd nanoparticles and the original surface silicon hydrides.

Compared to other well-known CO_2 hydrogenation catalysts, Pd@SiNS works under much milder conditions (27 p.s.i. and 170 °C). As far as we know, there is no report on Cu/SiO_2 or Cu/ZnO catalysing CO_2 reduction under 27 p.s.i. at 170 °C. These catalysts usually work under high-temperature and high-pressure conditions to catalyse CO_2 hydrogenation to methanol. The selectivity towards methanol increases as the reaction temperature becomes higher[20]. Even under 30 bar, the CO production rate on a Cu/ZnO/Al_2O_3 catalyst is still very low[21]. Neither does the other known catalyst, Pd@SiO_2, show any activity under such a mild condition[19]. With mild CO_2 reduction reaction conditions, facile catalyst preparation methods using low-cost $CaSi_2$ and stable performance under both batch and flow reactor conditions, the industrial viability of this catalyst holds substantial promise.

In situ diffuse reflectance infrared Fourier transform spectroscopy studies and the catalytic mechanism. To dig deeper into the CO_2 reduction reaction over Pd@SiNS, and to gain more mechanistic insights, we conducted in situ diffuse reflectance infrared Fourier transform spectroscopy (DRIFTS) studies with deuterium labelling. The Pd@SiNS sample was treated in the DRIFTS sample holder under a series of consecutive reaction conditions: (1) in CO_2/He (1:1) atmosphere at 170 °C for 1 h, (2) in D_2 at 170 °C for 2 h (in dark), (3) in D_2 at 170 °C for 1 h (in light). Exactly the same conditions were then applied to the control sample SiNS. The DRIFTS data were recorded as differential absorption spectra, so that the evolution of all the infrared active surface species could be tracked in real time. (Fig. 4a,b). Deuterium labelling in this experiment could help tell if the hydrogen in the surface hydroxide or surface hydride was coming from the H_2 gas during the catalytic reaction. In the classical picture of a stretching covalent bond as a harmonic oscillator, the vibrational frequency inversely scales with the square root of the reduced mass of the oscillator. In the case of D substituting H in surface silicon hydrides or hydroxides, the frequency would be reduced by a factor of $\sim\sqrt{2}$ (the actual factor[22] is ~1.37–1.38).

For Pd@SiNS, during the first hour of exposure to CO_2 there was a moderate decrease in the Si–H region at ~2,100 cm^{-1}, corresponding to surface hydrides initially consumed by CO_2, as described in equation (1). A slight loss of surface hydroxides was also observed, which was due to the dehydration reaction of these hydroxides at such an elevated temperature. It was when Pd@SiNS started to be exposed to D_2 that more peaks underwent dramatic changes. During the first 2 h in the dark, we observed a slight loss of surface oxides (Si–O–Si, at ~1,100 cm^{-1}), a moderate loss of hydrides (Si–H, at ~2,100 cm^{-1}) and a significant loss of hydroxides (Si–O–H, a broad peak at ~3,100–3,700 cm^{-1}), due to the reactions described in equations (4), (5) and (8) in Fig. 4c. Meanwhile, there were significant gains in surface deuteroxides (Si–O–D, at ~2,300–2,750 cm^{-1}) and surface deuterides (Si–D, at ~1,600 cm^{-1}) (red spectral line in Fig. 4a). After the final 1 h in light, the surface lost significantly more surface hydrides (Si–H) and surface oxides (Si–O–Si), and gained more surface deuterides (Si–D), and new peaks associated with surface

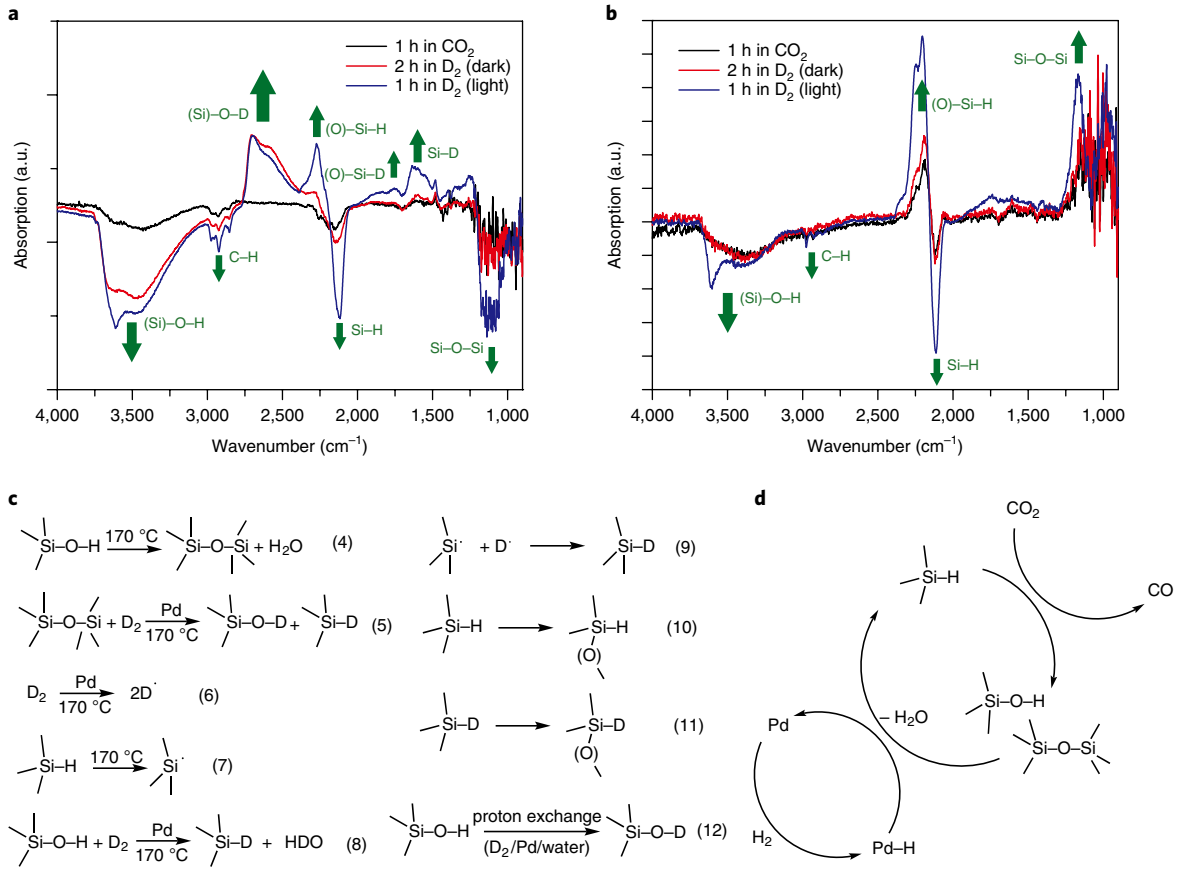

Fig. 4 | Isotope labelled in situ DRIFTS experiments and interpretation (catalytic mechanism). a,**b**, In situ DRIFTS spectra of Pd@SiNS (**a**) and pristine SiNS (**b**) samples under a series of consecutive reaction conditions, starting from reacting with CO_2 for 1 h, then with D_2 in the dark for 2 h, and finally with D_2 in light for 1 h, all at 170 °C, with corresponding spectral lines in black, red and blue, respectively, all of which are recorded as differential absorption spectra in a helium atmosphere. **c**, Key reactions involved in Pd@SiNS-catalysed CO_2 reduction that can be detected by isotope labelling. **d**, Catalytic cycle for CO_2 reduction with Pd@SiNS.

deuterides adjacent to an inserted backbone oxygen ((O)–Si–D, at ~1,750 cm^{-1}) emerged (blue spectral line in Fig. 4a), as described in equation (11) in Fig. 4c. Other information extracted from the spectra included a loss of adventitious surface organics (at ~2,850–2,980 cm^{-1}) and a moderate O insertion in the Si backbone neighbouring a surface hydride (at ~2,270 cm^{-1}), as described in equation (10) in Fig. 4c. This phenomenon was partially responsible for the loss of hydrides as seen in the spectra. According to these results, a quick conclusion could be drawn that for Pd@SiNS, D_2 was able to reduce the surface oxide and hydroxides under heat and light, yielding deuteroxides and deuterides.

In contrast, when the pristine SiNS sample without Pd nanoparticles was placed in the in situ DRIFTS spectrometer under the same conditions, there was little sign of surface deuteride formation and no sign of surface deuteroxide formation. The surface silicon hydrides, however, were consumed. This clearly indicated that D_2 was unable to reduce the surface oxide and hydroxides without the presence of Pd nanoparticles (equations (5) to (7) and (9) in Fig. 4c). Therefore, unlike Pd@SiNS, SiNS would fail in replenishing the surface hydrides and be unable to facilitate the catalytic cycle in this CO_2 reduction reaction.

According to the DRIFTS differential spectra for Pd@SiNS, we made a summary of the reactions involved and proposed a scheme for the catalytic cycle of the CO_2 reduction reaction on the Pd@SiNS surface (Fig. 4d). In this cycle, Si–H is oxidized by CO_2 and turns into surface oxidation species Si–OH and Si–O–Si. In the meantime, CO_2 is reduced to CO. On the other hand, the surface oxidation species Si–OH and Si–O–Si, once generated, are reduced by H· from the Pd-related H· source (equation (6) in Fig. 4c) and reinstated to surface hydrides, Si–H. This was experimentally supported by the intensity decrease of the Si–O–Si peak (blue line in Fig. 4a). This is the key step to complete the catalytic cycle, realized by the design of a Pd and Si nanosheet complex. It is worth noting that the reverse of this reaction (water gas shift reaction) could be catalysed as well, with the pathway and experimental support shown in Supplementary Figs. 10 and 11.

The Pd nanoparticle, as a H· source, is not the only factor that contributes to completion of the catalytic cycle. The function of the Si nanosheet as a support is equally important. Pd@oxSiNS showed no catalytic activity, because the support used in that case (wide-bandgap silica) was non-reducible, even in the presence of Pd. We also carried out an in situ DRIFTS study on the Pd@oxSiNS sample under the same conditions as we used with Pd@SiNS and the pristine SiNS. As expected, we still saw H–D exchange in the differential spectra, but we did not observe any decrease in the Si–O–Si region, nor Si–D emergence (Supplementary Fig. 7). The surface H–D exchange could happen in the presence of Pd and water via a proton exchange process, as described in equation (12) in Fig. 4c[23–25]. However, the slightly oxidized surface of Pd@SiNS is reducible. The Si nanosheet support has a significant amount of surface defects. The adventitious surface oxides are more strained compared to the Si–O bonds in a bulk (or fully oxidized) silica sample. Recent ab initio modelling has shown that the breaking of the strained surface Si–O bonds by zero-valence H atoms is energetically favourable,

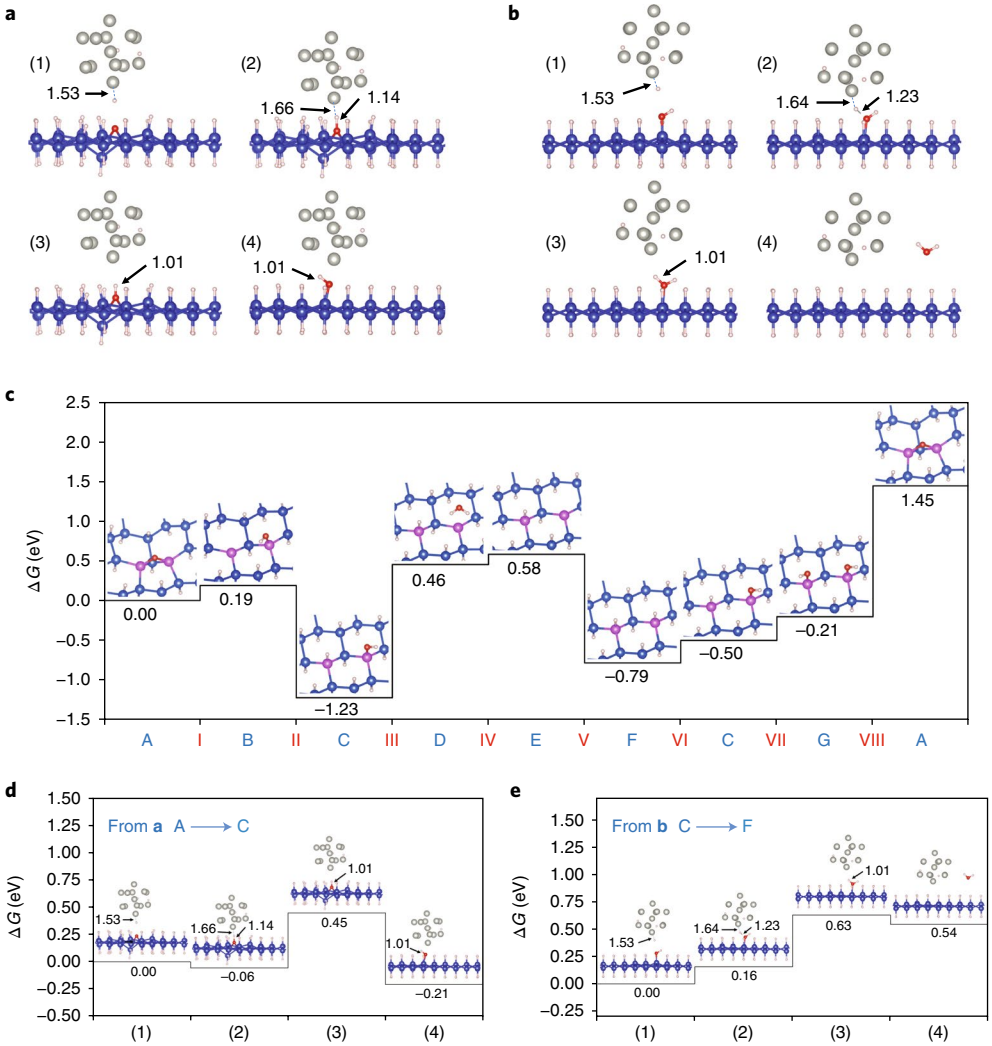

Fig. 5 | DFT simulation results. a, Mode of interaction of a 13 Pd atom nanoparticle (NP) with a surface hydride (Pd–H) and a surface oxide (Si–O–Si): (1) initial step; (2) interaction of the H atom with both NP and SiNS; (3) normal bonding of the H atom to the surface Si–O–Si; (4) breakage of one of the Si–O bonds. **b**, Mode of interaction of the Pd nanoparticle (Pd–H) with a surface hydroxyl (Si–OH): (1) initial step; (2) interaction of the H atom with both NP and SiNS; (3) normal bonding of the H atom to the surface Si–OH; (4) desorption of H_2O. **c**, Free energy profile of the Si surface at different stages of the catalytic cycle. **d**, Free energy profile associated with the transfer of H from the Pd nanoparticle to the Si–O–Si site. **e**, Free energy profile associated with the transfer of H from the Pd nanoparticle to the Si–OH site. Grey, red, white, blue and pink balls indicate Pd, O, H, Si and interacting Si atoms, respectively.

reducing the surface to a hydride site and a hydroxide site[26]. Our experimental data are consistent with these predictions. Moreover, when the sample is under illumination, this reduction process could be aided by the photothermal effect of Pd nanoparticles. The local temperature of the Pd nanoparticles and their vicinity can be much higher than the sample embedded-thermocouple-measured temperature[27]. Therefore, the regeneration of surface hydrides could be accelerated kinetically.

DFT simulations. Spin-polarized DFT calculations were performed to investigate the reactions over Pd@SiNS. Si nanosheet bonds, including surface hydrides (Si–H), surface oxides (Si–O–Si) and surface hydroxyls (Si–OH) were analysed, and the interactions between surface Si–H, Si–O–Si and Si–OH constituents with H atoms adsorbed on the Pd nanoparticles were modelled by clusters of 13 Pd atoms, consistent with previous studies[28–31]. Figure 5a,b present schematics for the transfer of H atoms from the Pd nanoparticle to the surface Si–O–Si and Si–OH, respectively, calculated by DFT geometric optimization, which suggest each H transfer takes place in four steps.

Our geometry optimization calculations for pristine SiNS show that, while the presence of surface Si–O–Si highly deforms the plane nanosheet (Supplementary Fig. 8a), surface Si–OH does not affect the planarity of the nanosheet (Supplementary Fig. 8b).

As illustrated in Fig. 5a, at the beginning of H bonding to the surface oxide, the optimized Pd nanoparticle structure involves an atomic distance of 1.53 Å between Pd and H atoms, while it increases in step 2 to 1.66 Å when bonding to Si–O–Si, resulting in an O–H bond length of 1.14 Å. In the next step, the bond length decreases to 1.01 Å (due to the strong O–H interaction) and switches to a normal hydroxide bonding. This is followed by a bond breakage at one of the O–Si bonds of Si–O–Si, which finally leads to the creation of a Si–OH and a radical on the surface. On the other hand, when the Si–OH interacts with a H atom of a Pd nanoparticle, the optimized distance between the Pd and the H atom becomes 1.64 Å at step 2, and the H atom forms a weak H–OH with a bond length of 1.23 Å. At step 3, H makes a stronger H–OH bond with a length of 1.01 Å, which is the same as the bond length of the initial OH group, leading to desorption of the water molecule at step 4.

It is worthwhile to note that the interaction of the Pd surface with H_2 molecules has been extensively studied by both theory and experiment[32–34]. This process involving the breakage of the H_2 bond and the adsorption of H atoms on the Pd surface has a small energy barrier, which can be less than 0.1 eV (refs. [35,36]). Therefore, our investigation into the catalytic cycle only includes the possible reactions between the silicane nanosheet and the hydrogen, CO_2 and H_2O.

As shown in Fig. 5c, the total energy change for the reaction Si–O–Si + 2 H → Si–OH + Si-H (reaction (1)) is −1.23 eV and shows the exothermic nature of this reaction, while the energy variation for the reaction Si–OH + Si-H + 2 H → Si–H + Si–H + H_2O (reaction (2)) is +0.44 eV and exhibits endothermic behaviour. Moreover, Fig. 5c suggests that the last step (step VIII) is the most endothermic step, including an energy absorption of +1.66 eV. These steps can also be presented in a cycle, as shown by Supplementary Fig. 12.

The energetic behaviour of both reactions was also investigated and confirmed by another set of simulations carried out to study the direct interactions between the Pd particle and the Si nanosheet. Figure 5d illustrates the free energy profile associated with the transfer of H from the Pd nanoparticle to the active site on the Si–O–Si surface. This corresponds to step A → C of Fig. 5c. Figure 5e illustrates the free energy profile associated with the transfer of H from the Pd nanoparticle to the Si–OH site, which corresponds to step C → F of Fig. 5c. The results showed that with the presence of Pd, the process from A to C was less exothermic and the one from C to F was less endothermic.

In summary, consistent with experimental results, the DFT calculations suggest that the H transfer process from Pd to the oxidized SiNS surface may occur repeatedly by two mechanisms. First, a H atom adsorbed on the nanoparticle interacts with a surface Si–O–Si and creates a Si–OH; second, another H from the nanoparticle forms a bond with the Si–OH, which leads to the desorption of water, creating a surface radical, thereby enabling a catalytic cycle. The strain induced in the SiNS by the Si–O–Si bonds is probably responsible for the enhanced reactivity of the oxidized SiNS surface towards catalytic hydrogenation of CO_2 under mild conditions.

Conclusion

In the quest to achieve catalytic reduction of carbon dioxide by surface silicon hydrides, we have designed and synthesized Pd-nanoparticle-decorated Si nanosheets (Pd@SiNS). The synthesis of Pd@SiNS follows the general and facile synthetic strategy of fast metal nanoparticle growth on the surface of hydride-capped Si nanosheets.

The Pd@SiNS sample had a ^{13}CO production rate of 10,000 nmol $(g\ cat)^{-1}\ h^{-1}$. The rate remained at this level during long cycles. In comparison, the pristine SiNS sample showed lower ^{13}CO production rates that dropped more quickly and were unstable. Another control experiment showed that Pd on a fully oxidized Si nanosheet (Pd@oxSiNS) had a zero ^{13}CO production rate, which demonstrated the negligible contribution of Pd nanoparticles themselves for CO_2 reduction, and suggested a synergetic effect of Pd and the Si nanosheet surface in the case of Pd@SiNS.

The in situ DRIFTS study with isotope labelling helped in understanding how we established the missing link in the catalytic cycle by the synergy of the Si nanosheet surface and Pd. By probing the evolution of the surface species while mimicking the actual CO_2 reduction conditions, we found that in the presence of Pd, the Si nanosheet surface oxides and hydroxides can be reduced by H_2, reinstating surface hydrides. The DFT simulation results were consistent with the experimental observations, giving us insights into how and why Pd–H reacts with surface oxides and hydroxides on the Si nanosheet surface. Oxidation-induced ring strain in the Si nanosheets appears to be the cause of the enhanced reactivity compared to the Si nanocrystals.

This study not only provides inspiration for the future design and development of new heterogeneous CO_2 catalysts, but also updates the basic understanding of Si surface chemistry.

Methods

Synthesis of SiNS and Pd@SiNS. In a typical synthesis of SiNS, 1.0 g of calcium silicide powder (Fluka) was dispersed in 100 ml hydrochloric acid (36%, Caledon Laboratory Chemicals) precooled to −25 °C. The reaction was carried out in a jacketed flask with two hose connections for circulating medium (ethylene glycol/water) pumped through a NESLAB RTE-111 refrigerated bath circulator. The reaction temperature was kept between −15 °C to −20 °C. The mixture was stirred under an inert atmosphere for 7 days. The liquid in the reaction mixture was then removed in a funnel and the solid product (unetched SiNS) was collected and washed with anhydrous acetone and dried under vacuum.

A typical synthesis of Pd@SiNS started from the etching of SiNS: 30 mg of unetched SiNS power was dispersed in 5 ml EtOH and sonicated for 1 min. Deionized (DI) water (2 ml) and 0.25 ml of hydrofluoric acid (48%, Sigma-Aldrich) were subsequently added to the dispersion. The mixture was stirred for 1.5 min. After a 1 min centrifugation, the supernatant containing hydrofluoric acid was dumped and the solid product was collected. The product (etched SiNS, H-terminated) was washed in acetone three times.

To synthesize a 0.5% loading of Pd@SiNS, 5 mg of palladium acetate was dissolved in 1 ml of acetone and diluted 100 times. A 1 ml volume of the diluted palladium acetate solution was then added to a dispersion of etched SiNS containing 5 mg of SiNS and 1.5 ml acetone at room temperature. The mixture was then agitated with simultaneous vortex and sonication for 2 min. The product (Pd@SiNS) was kept in acetone to minimize exposure to ambient air. Control samples of 5–10 nm Pd nanoparticles and 2–4 nm Pd@SiO_2 were also synthesized at room temperature via a reduction method[37], using Pd salts, $NaBH_4$ and a commercially available SiO_2 support (Aldrich, fumed, powder, 0.007 μm).

Material characterizations. PXRD was performed on a Bruker D2-Phaser X-ray diffractometer, using Cu K_α radiation at 30 kV. The nitrogen sorption experiments were performed at 77 K on a Quantachrome Autosob-1-C instrument. Before each adsorption measurement the samples were degassed at 60 °C overnight under vacuum. The specific surface area was determined using the BET equation, applied to the best linear fit within the range of $0.05 \leq P/P_0 \leq 0.35$. FTIR was performed using a Perkin Elmer Spectrum-One FTIR fitted with a universal attenuated total reflectance sampling accessory with a diamond-coated zinc-selenide window. Diffuse reflectance of the samples was measured using a Lambda 1050 UV/vis/NIR spectrometer from Perkin Elmer and an integrating sphere with a diameter of 150 mm. The STEM images of the Pd@SiNS sample were taken on a Hitachi S-5200 high-resolution 'in lens' scanning electron microscope with an STEM detector. The energy-dispersive X-ray (EDX) mapping was performed with an Oxford Inca EDX system. XPS was performed in an ultrahigh-vacuum chamber with a base pressure of 10^{-9} torr. The system used a Thermo Scientific K-Alpha XPS spectrometer, with an Al K_α X-ray source operating at 12 kV, 6 A and X-ray wavelength of 1,486.7 eV. The spectra were obtained with an analyser pass energy of 50 eV and an energy spacing of 0.1 eV. The sample for XPS analysis was prepared by dropcasting a Pd@SiNS dispersion in acetone on carbon substrates and left in vacuum for several hours. Data analysis was carried out using Thermo Scientific Avantage software.

Gas-phase CO_2 reduction tests. Borosilicate glass microfibre filters were used as substrates for gas-phase reaction measurements to guarantee a high surface area as well as mechanical stability. A fresh dispersion of Pd@SiNS (0.5% mass loading) in acetone was dropped onto the filters and dried under N_2 flow to yield films containing ~1 mg Pd@SiNS. The films were dried further under vacuum overnight, before being put into the reactor. A total pressure of ~27 p.s.i., a constant temperature of 170 °C and irradiation with a 300 W Xe lamp (Newport, Model 67005, light intensity of ~15 suns) for 2.3 h were the standard conditions for each run (unless stated for specific cases elsewhere in the Article). The custom-fabricated stainless-steel batch reactor had a volume of 11.8 ml, with a fused-silica view port sealed with Viton O-rings. The reactors were evacuated using an Alcatel dry pump before being purged with the reactant gases H_2 (99.9995%) and CO_2 (99.999%) at a flow rate of 6 ml min^{-1} and a stoichiometry of 1:1 (stoichiometric for reverse water gas shift reaction). During purging, the reactors were sealed once they had been heated to the desired temperature. The reactor temperatures were controlled by an OMEGA CN616 6-Zone temperature controller combined with a thermocouple placed in contact with the sample. The pressure inside the reactor was monitored during the reaction using an Omega PX309 pressure transducer during the reaction. Product gases were analysed with a flame ionization detector (FID) and a thermal conductivity detector (TCD) installed in a SRI-8610 gas chromatograph (GC) with a 3′ Mole Sieve 13a and a 6′ Haysep D column. Isotope tracing experiments were performed using $^{13}CO_2$ (99.9 at%, Sigma Aldrich). The reactors were evacuated before being injected with $^{13}CO_2$, followed by H_2. Isotope product gases were measured using an Agilent 7890A gas chromatographic mass spectrometer (GC-MS) with a 60 m GS-CarbonPLOT column fed into the mass spectrometer. The ^{13}CO production rates were calculated according to the total CO

production rates and the ratio of the integrated GC peak areas of ^{13}CO and ^{12}CO. Peak analysis was performed using OriginPro 8.5 (OriginLab).

In situ DRIFTS studies. The in situ DRIFTS experiments were performed on a Thermo Scientific Nicolet iS50 FTIR spectrometer with a mercury cadmium telluride (MCT) detector cooled with liquid nitrogen. The spectrometer was equipped with a Harrik Praying Mantis diffuse reflection accessory and a Harrick high-temperature reaction chamber (HTC) with ZnSe windows (Supplementary Fig. 9). The temperature was controlled by a Harrick ATC-024–3 temperature controller. Automated temperature changes were programmed with Watlow EZ-Zone Configurator software. The sample was illuminated by a 120 W Xe lamp (Newport, Model 67005) at a distance where the light intensity on the sample was kept at ~4 suns. Spectrometer data were obtained using OMNIC software (Thermo Scientific). The autosampling function in the OMNIC software was used to collect data at specific time intervals. The loaded sample in the HTC was pressed for 20 s to ensure a flat and even surface. The following procedure for data collection was used. The sample was purged for 40 min at 170 °C in He (15 s.c.c.m.). The sample was cooled to 50 °C to collect background data, so the spectra collected afterwards were differential spectra. CO_2 was introduced to the sample with He for 1 h at 170 °C. The sample was then flushed with helium only for 40 min at 50 °C to remove CO_2. The reactant gas D_2 and He were subsequently flowed for 2 h at 170 °C in the dark. The He was flushed for 40 min at 50 °C to remove D_2. For reaction under light the sample was then reacted with D_2 at 170 °C with Xe lamp illumination for 1 h. Finally, the He was used to flush the chamber at 50 °C for 40 min. During the procedure, the flow of He was constant and unchanged. The flow rate of all gases was 15 s.c.c.m.

DFT simulations. Spin-polarized DFT simulations were conducted using the Vienna Ab-initio Simulation Package (VASP)[38]. Projector augmented-wave[39] pseudo-potentials with Perdew–Burke–Ernzerhof[40] exchange-correlation functional were utilized. The kinetic energy cutoff and the electron self-consistent criterion were considered to be 500 eV and 10^{-4}, respectively, and a Hellmann–Feynman force threshold of 1×10^{-2} eV Å^{-1} was selected. Grimme's semi-empirical correction scheme[41] was applied to modify the exchange-correlation energy calculations[42,43].

To study the interaction of the Si surface and the Pd particle, silicene slabs involving 60 Si atoms and a supercell of $4\times3\times1$ unit cells were passivated by different numbers of surface H, O and OH constituents, and Pd spherical particles consisting of 13 Pd atoms embedding various H coverages were modelled. To avoid the orbital interaction in the z direction, a vacuum space of 30 Å was considered. To obtain nanosheet and nanoparticle structures they were optimized separately, then placed in a single simulation box with dimensions of $a=15.28$ Å and $b=19.854$ Å to monitor the interactions. To integrate quantities over the Brillouin zone, a Monkhorst–Pack mesh of $4\times4\times1$ was selected and the first-order Methfessel–Paxton with a width of 0.1 eV was used as the smearing scheme. The Cartesian coordinates of the optimized models are provided in the Supplementary Data Set.

Data availability

The data that support the findings of this study are available from the corresponding author upon reasonable request.

Received: 8 March 2018; Accepted: 9 November 2018;
Published online: 31 December 2018

References

1. Faunce, T. A. et al. Energy and environment policy case for a global project on artificial photosynthesis. *Energy Environ. Sci.* **6**, 695–698 (2013).
2. Goeppert, A., Czaun, M., Jones, J.-P., Surya Prakash, G. K. & Olah, G. A. Recycling of carbon dioxide to methanol and derived products—closing the loop. *Chem. Soc. Rev.* **43**, 7995–8048 (2014).
3. Rongé, J. et al. Monolithic cells for solar fuels. *Chem. Soc. Rev.* **43**, 7963–7981 (2014).
4. Ozin, G. A. Throwing new light on the reduction of CO_2. *Adv. Mater.* **27**, 1957–1963 (2015).
5. Zubrin, R., Wagner, R. & Clarke, A. C. *The Case for Mars* (Free Press, New York, 2011).
6. Matsuo, T. & Kawaguchi, H. From carbon dioxide to methane: homogeneous reduction of carbon dioxide with hydrosilanes catalyzed by zirconium–borane complexes. *J. Am. Chem. Soc.* **128**, 12362–12363 (2006).
7. Berkefeld, A., Piers, W. E. & Parvez, M. Tandem frustrated Lewis pair/tris(pentafluorophenyl)borane-catalyzed deoxygenative hydrosilylation of carbon dioxide. *J. Am. Chem. Soc.* **132**, 10660–10661 (2010).
8. Riduan, S. N., Ying, J. Y. & Zhang, Y. Mechanistic insights into the reduction of carbon dioxide with silanes over N-heterocyclic carbene catalysts. *ChemCatChem* **5**, 1490–1496 (2013).
9. Dasog, M. et al. Size vs surface: tuning the photoluminescence of freestanding silicon nanocrystals across the visible spectrum via surface groups. *ACS Nano* **8**, 9636–9648 (2014).
10. Sun, W. et al. Heterogeneous reduction of carbon dioxide by hydride-terminated silicon nanocrystals. *Nat. Commun.* **7**, 12553 (2016).
11. Wong, A. P. Y. et al. Tailoring CO_2 reduction with doped silicon nanocrystals. *Adv. Sustain. Syst.* **1**, 1700118 (2017).
12. Dasog, M., Kraus, S., Sinelnikov, R., Veinot, J. & Rieger, B. CO_2 to methanol conversion using hydride terminated porous silicon nanoparticles. *Chem. Commun.* **53**, 3114–3117 (2017).
13. Nakano, H. et al. Soft synthesis of single-crystal silicon monolayer sheets. *Angew. Chem. Int. Ed.* **45**, 6303–6306 (2006).
14. Chandra, S., Masuda, Y., Shirahata, N. & Winnik, F. M. Transition-metal-doped NIR-emitting silicon nanocrystals. *Angew. Chem. Int. Ed.* **56**, 6157–6160 (2017).
15. Zhang, Y. et al. Tunable metal/silicon hybrid dots catalysts for hydrocarbon selective oxidation. *J. Phys. Chem. C* **116**, 20363–20367 (2012).
16. Albers, P., Pietsch, J. & Parker, S. F. Poisoning and deactivation of palladium catalysts. *J. Mol. Catal. A* **173**, 275–286 (2001).
17. Martins, J. et al. CO_2 hydrogenation with shape-controlled Pd nanoparticles embedded in mesoporous silica: elucidating stability and selectivity issues. *Catal. Commun.* **58**, 11–15 (2014).
18. Daza, Y. A. & Kuhn, J. N. CO_2 conversion by reverse water gas shift catalysis: comparison of catalysts, mechanisms and their consequences for CO_2 conversion to liquid fuels. *RSC Adv.* **6**, 49675–49691 (2016).
19. Ye, J., Ge, Q. & Liu, C. Effect of PdIn bimetallic particle formation on CO_2 reduction over the Pd–In/SiO_2 catalyst. *Chem. Eng. Sci.* **135**, 193–201 (2015).
20. Wang, Z.-Q. et al. High-performance and long-lived Cu/SiO_2 nanocatalyst for CO_2 hydrogenation. *ACS Catal.* **5**, 4255–4259 (2015).
21. Kunkes, E. L., Studt, F., Abild-Pedersen, F., Schlögl, R. & Behrens, M. Hydrogenation of CO_2 to methanol and CO on Cu/ZnO/Al_2O_3: is there a common intermediate or not? *J. Catal.* **328**, 43–48 (2015).
22. McKean, D. C. On the assignment of SiH and SiD stretching frequencies: a reanalysis of the ν_7 bands of Si_2H_6 and Si_2D_6 and a harmonic local mode force field for disilane. *Spectrochim. Acta A Mol. Spectrosc.* **48**, 1335–1345 (1992).
23. Benson, J. E., Kohn, H. W. & Boudart, M. On the reduction of tungsten trioxide accelerated by platinum and water. *J. Catal.* **5**, 307–313 (1966).
24. Levy, R. B. & Boudart, M. The kinetics and mechanism of spillover. *J. Catal.* **32**, 304–314 (1974).
25. Baumgarten, E. & Denecke, E. Hydrogen spillover in the system Pt Al_2O_3. I. Fundamental observations. *J. Catal.* **95**, 296–299 (1985).
26. El-Sayed, A. M., Watkins, M. B., Grasser, T., Afanas'Ev, V. V. & Shluger, A. L. Hydrogen-induced rupture of strained SiO bonds in amorphous silicon dioxide. *Phys. Rev. Lett.* **114**, 115503 (2015).
27. Jia, J. et al. Photothermal catalyst engineering: hydrogenation of gaseous CO_2 with high activity and tailored selectivity. *Adv. Sci.* **4**, 1700252 (2017).
28. Silaghi, M. C., Comas-Vives, A. & Copéret, C. CO_2 activation on Ni/γ-Al_2O_3 catalysts by first-principles calculations: from ideal surfaces to supported nanoparticles. *ACS Catal.* **6**, 4501–4505 (2016).
29. Bartolomé, J. et al. Magnetization of Pt_{13} clusters supported in an NaY zeolite: a XANES and XMCD study. *Phys. Rev. B* **80**, 014404 (2009).
30. Ewing, C. S., Veser, G., McCarthy, J. J., Johnson, J. K. & Lambrecht, D. S. Effect of support preparation and nanoparticle size on catalyst–support interactions between Pt and amorphous silica. *J. Phys. Chem. C* **119**, 19934–19940 (2015).
31. Di Paola, C., Pavan, L., D'Agosta, R. & Baletto, F. Structural stability and uniformity of magnetic Pt_{13} nanoparticles in NaY zeolite. *Nanoscale* **9**, 15658–15665 (2017).
32. Dong, W. & Hafner, J. Dissociative adsorption on Pd(111). *Phys. Rev. B* **56**, 15396–15403 (1997).
33. Liu, D., Gao, Z. Y., Wang, X. C., Zeng, J. & Li, Y. M. DFT study of hydrogen production from formic acid decomposition on Pd–Au alloy nanoclusters. *Appl. Surf. Sci.* **426**, 194–205 (2017).
34. Johansson, M. et al. Hydrogen adsorption on palladium and palladium hydride at 1 bar. *Surf. Sci.* **604**, 718–729 (2010).
35. Resch, C., Berger, H. F., Rendulic, K. D. & Bertel, E. Adsorption dynamics for the system hydrogen/palladium and its relation to the surface electronic-structure. *Surf. Sci.* **316**, L1105–L1109 (1994).
36. Dong, W., Kresse, G. & Hafner, J. Dissociative adsorption of H_2 on the Pd(111) surface. *J. Mol. Catal. A* **119**, 69–76 (1997).
37. Leopold, K., Maier, M. & Schuster, M. Preparation and characterization of Pd/Al_2O_3 and Pd nanoparticles as standardized test material for chemical and biochemical studies of traffic related emissions. *Sci. Total Environ.* **394**, 177–182 (2008).
38. Kresse, G. & Furthmüller, J. Efficient iterative schemes for ab initio total-energy calculations using a plane-wave basis set. *Phys. Rev. B* **54**, 11169–11186 (1996).
39. Kresse, G. & Joubert, D. From ultrasoft pseudopotentials to the projector augmented-wave method. *Phys. Rev. B* **59**, 1758 (1999).
40. Perdew, J. P., Burke, K. & Ernzerhof, M. Generalized gradient approximation made simple. *Phys. Rev. Lett.* **77**, 3865–3868 (1996).

41. Grimme, S. Semiempirical GGA-type density functional constructed with a long-range dispersion correction. *J. Comput. Chem.* **27**, 1787–1799 (2006).
42. Bučko, T., Hafner, J., Lebègue, S. & Ángyán, J. G. Improved description of the structure of molecular and layered crystals: ab initio DFT calculations with van der Waals corrections. *J. Phys. Chem. A* **114**, 11814–11824 (2010).
43. Wang, Z., Selbach, S. M. & Grande, T. Van der Waals density functional study of the energetics of alkali metal intercalation in graphite. *RSC Adv.* **4**, 4069–4079 (2014).

Acknowledgements

G.A.O. acknowledges financial support from the Ontario Ministry of Research and Innovation (MRI), the Ministry of Economic Development, Employment and Infrastructure (MEDI), the Ministry of the Environment and Climate Change's (MOECC) Best in Science (BIS) Award, Ontario Center of Excellence Solutions 2030 Challenge Fund, Ministry of Research Innovation and Science (MRIS) Low Carbon Innovation Fund, Imperial Oil, the University of Toronto's Connaught Innovation Fund (CIF), Connaught Global Challenge (CGC) Fund and the Natural Sciences and Engineering Research Council of Canada (NSERC). C.Q. and W.S. acknowledge the Connaught Fund and Department of Chemistry at the University of Toronto for funding. M.M. and C.V.S. acknowledge financial support in part by the Natural Sciences and Engineering Council of Canada (NSERC), University of Toronto, Connaught Global Challenge Award and Hart Professorship. The computations were carried out using University of Toronto computers and Compute Canada facilities, particularly SciNet and Calcul-Quebec. The authors acknowledge continued support from these supercomputing facilities. The authors thank X.Yan for helpful discussions on materials characterizations.

Author contributions

C.Qian, W.S. and G.A.O. conceived and designed the experiments. C.Qian, W.S., D.L.H.H. and S.G.H.K. prepared the materials and carried out the batch and flow experiments. C.Qian, W.S., C.Qiu and L.Wan. prepared the materials and carried out the batch with high-intensity light experiments. M.M. conducted DFT simulations under the supervision of C.V.S., and together they did the analysis and discussed the simulation data with C.Qian, W.S., M.G. and G.A.O. With the support of T.E.W., C.Qian, W.S. and D.L.H.H. performed the in situ DRIFTS study. A.A.T. conducted the Aspen simulation and estimated the equilibrium composition. Y.F.L. and I.G. performed SEM and TEM characterizations. M.X. and L.Wang performed XPS characterizations. Y.D. carried out the nitrogen sorption study. C.Qian, W.S. and G.A.O. co-wrote the manuscript. All authors discussed the results and commented on the manuscript.

Competing interests

The authors declare no competing interests.

Additional information

Supplementary information is available for this paper at https://doi.org/10.1038/s41929-018-0199-x.

Reprints and permissions information is available at www.nature.com/reprints.

Correspondence and requests for materials should be addressed to C.V.S. or G.A.O.

Publisher's note: Springer Nature remains neutral with regard to jurisdictional claims in published maps and institutional affiliations.